8-2018

Probing High-Momentum Protons and Neutrons in Neutron-Rich Nuclei

The CLAS Collaboration

L. B. Weinstein

S. Bültmann

D. Bulumulla

G. Charles

See next page for additional authors

Authors
The CLAS Collaboration, L. B. Weinstein, S. Bültmann, D. Bulumulla, G. Charles, G. Dodge, F. Hauenstein, C. E. Hyde, A. Klein, S. Nadeeshani, Y. Prok, and Z. W. Zhao

LETTER

https://doi.org/10.1038/s41586-018-0400-z

Probing high-momentum protons and neutrons in neutron-rich nuclei

The CLAS Collaboration*

The atomic nucleus is one of the densest and most complex quantum-mechanical systems in nature. Nuclei account for nearly all the mass of the visible Universe. The properties of individual nucleons (protons and neutrons) in nuclei can be probed by scattering a high-energy particle from the nucleus and detecting this particle after it scatters, often also detecting an additional knocked-out proton. Analysis of electron- and proton-scattering experiments suggests that some nucleons in nuclei form close-proximity neutron–proton pairs[1–12] with high nucleon momentum, greater than the nuclear Fermi momentum. However, how excess neutrons in neutron-rich nuclei form such close-proximity pairs remains unclear. Here we measure protons and, for the first time, neutrons knocked out of medium-to-heavy nuclei by high-energy electrons and show that the fraction of high-momentum protons increases markedly with the neutron excess in the nucleus, whereas the fraction of high-momentum neutrons decreases slightly. This effect is surprising because in the classical nuclear shell model, protons and neutrons obey Fermi statistics, have little correlation and mostly fill independent energy shells. These high-momentum nucleons in neutron-rich nuclei are important for understanding nuclear parton distribution functions (the partial momentum distribution of the constituents of the nucleon) and changes in the quark distributions of nucleons bound in nuclei (the EMC effect)[1,13,14]. They are also relevant for the interpretation of neutrino-oscillation measurements[15] and understanding of neutron-rich systems such as neutron stars[3,16].

Since the 1950s, the independent-particle shell model has been an indispensable guide for understanding nuclei[17]. In this model, nucleons move independently in well defined quantum orbits (shells) with low momentum, k ($k < k_F$, where k_F is the Fermi momentum), similarly to electrons in atoms. The potential in which the nucleons move is the average nuclear field created by their mutual strong interactions. Although successful in making many important predictions, such as shell closures and the spins and parities of nuclear ground and excited states, this textbook picture of the nucleus is incomplete: electron-scattering experiments in nuclei ranging from lithium to lead measured only about 60%–70% of the expected number of protons in each shell[18]. Newer shell-model-type calculations include the effects of long-range correlations, increasing this fraction to about 80%[19].

Modern superconducting accelerators—with high energy, high intensity and high duty factor—enable experiments that use scattering reactions to resolve the structure and dynamics of individual nucleons and nucleon pairs in nuclei. The resolving power of a measurement is determined by its momentum transfer, and its interpretation relies on

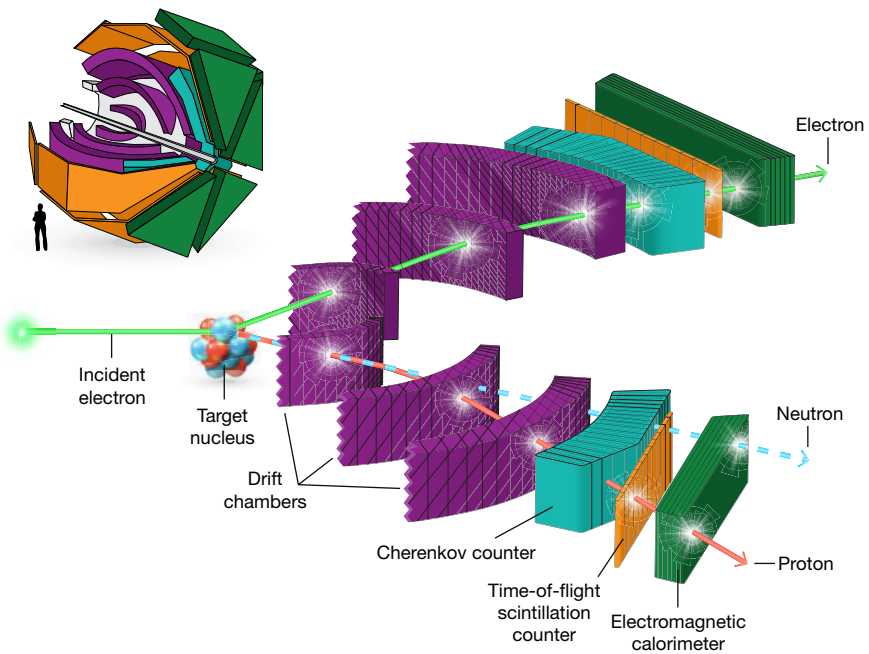

Fig. 1 | CLAS spectrometer. Two segments of the CLAS spectrometer. Electrons travelling with energies of up to 6 GeV hit nuclei, knocking out individual protons and neutrons. The momenta of the scattered electrons and knocked-out protons are reconstructed by analysing their trajectories as they bend in a toroidal magnetic field. The neutron momenta are deduced from their time of flight until they interact with the electromagnetic calorimeter. Inset, the almost-spherical CLAS. The electron beam travels along the grey pipe, hitting a target near the centre of the spectrometer.

*A list of authors and their affiliations appears at the end of the paper.

the theoretical modelling of the interaction, which should account for all possible mechanisms that lead to the same measured final state. The high-momentum transfer measurements reported here are discussed in terms of interaction with single nucleons, which is the simplest reaction picture that is consistent with the measured observables[1–3] and various ab initio calculations[20].

When analysed within this framework, electron-scattering experiments suggest that about 20% of the nucleons in nuclei have momentum greater than k_F[1–3,10–12]. These nucleons are absent in the one-body shell-model description of the data and are coupled into short-lived correlated nucleon pairs with large relative momentum ($k_{relative} > k_F \approx 250\,MeV\,c^{-1}$) and small centre-of-mass momentum (k_{CM}), referred to as short-range correlated (SRC) pairs[1–3].

The dominant force between nucleons in SRC pairs is tensor in nature[1,2]. This pair-wise interaction acts predominantly on spin-1 neutron–proton (*np*) SRC pairs, leading to a predominance of *np* SRC pairs over proton–proton (*pp*) and neutron–neutron (*nn*) SRC pairs by a factor of about 20. This phenomenon is referred to as '*np* dominance'[1–8].

Almost all high-momentum nucleons in nuclei belong to an SRC pair. As the short-distance interaction between nucleons in SRC pairs is very strong, the characteristics of the resulting pairs are largely independent of the rest of the nucleus. Thus, the distribution of high-momentum nucleons (the 'high-momentum tail' of the distribution) has a universal shape for all nuclei[1–3,9–11,21].

SRC pairs considerably complicate the nuclear ground state and nuclear-structure calculations. From a theoretical point of view, one can use a unitary transform to shift this complexity from the ground state to many-body interaction operators that describe the same measured final state[22,23], shifting the physics from high-momentum correlations to short-distance operators. The physical pictures of high-momentum nucleons and short-distance operators are based on the different momentum and distance scales of these effects from those of the shell model. The results reported here constrain short-distance phenomena, as described in either framework.

The analysis reported here was motivated by the quest to study the short-distance dynamics of protons and neutrons in neutron-rich nuclei. For the first time, we simultaneously measured electron-induced quasi-elastic knock-out of protons and neutrons from medium and heavy nuclei, using the A(e,$e'p$) and A(e,$e'n$) reactions, respectively (e, incident electron; e', scattered electron; A, target nucleus). The simultaneous measurement of both proton and neutron knock-out allows us to directly compare their properties using minimal assumptions. Analysed within the one-body reaction picture, the data from these measurements perform four functions: (1) quantifying the relative fractions of high-momentum ($k > k_F$) protons and neutrons, (2) showing that adding neutrons to the nucleus increases the fraction of high-momentum protons, (3) helping confirm the *np* dominance of the high-momentum tail in medium and heavy nuclei, and (4) supporting momentum-sharing inversion in heavy nuclei. In a more general framework, the data show that short-distance dynamics is similar in all nuclei, supporting a scale separation of short-distance physics from the nuclear shell model.

The data presented here were collected in 2004 in Hall-B of the Thomas Jefferson National Accelerator Facility (Jefferson Laboratory) in Virginia, USA, and were reanalysed as part of the data-mining initiative of the Jefferson Laboratory. The experiment used a 5.014 GeV electron beam incident on deuterium, carbon, aluminium, iron and lead targets, and the CEBAF (continuous electron beam accelerator facility) large acceptance spectrometer (CLAS)[24] to detect the scattered electrons and any associated hadrons knocked out during the interaction (see Fig. 1). CLAS used a toroidal magnetic field and six independent sets of drift chambers, time-of-flight scintillation counters, Cherenkov counters and electromagnetic calorimeters, covering scattering angles from about 8° to 140°, for charged-particle identification and trajectory reconstruction. The neutrons were identified by observing interactions in the forward electromagnetic calorimeters (covering about 8°–45°) with no associated charged-particle tracks in the drift chambers. The angle- and momentum-dependent neutron detection efficiency and momentum reconstruction resolution were measured simultaneously using the d(e,$e'p\pi^+\pi^-n$) reaction (d, deuterium; π, pion; see Supplementary Information). The experiment recorded all events with a scattered electron detected in both the electromagnetic calorimeter and the Cherenkov counter, along with any other particles.

High-energy electrons scatter from the nucleus by transferring a single virtual photon, carrying momentum $\boldsymbol{q}$ and energy ω. In quasi-elastic scattering, this momentum transfer is absorbed by a nucleon with initial momentum $\boldsymbol{p}_i$. If the nucleon does not rescatter as it leaves the nucleus, then it will emerge with final momentum $\boldsymbol{p}_f = \boldsymbol{p}_i + \boldsymbol{q}$. Thus, we can reconstruct the approximate initial momentum of the nucleon from the missing momentum, namely, the difference between the detected final momentum and the transferred momentum: $\boldsymbol{p}_{miss} = \boldsymbol{p}_f - \boldsymbol{q}$. Similarly, the excitation energy of the residual (A−1) nucleus is related to the missing energy, $E_{miss} = \omega - T_f$, where T_f is the nucleon's kinetic energy.

Although this quasi-elastic picture of the scattering reaction is highly intuitive and consistent with the measured observables, other reaction mechanisms using two-body currents that result in the same measured final state are added coherently and cannot be distinguished from the quasi-elastic mechanism. Contribution from non-quasi-elastic reaction mechanisms is minimized by the use of large momentum transfer and the specific reaction kinematics used in the measurement (see Methods). In addition, these effects are further diminished by forming cross-section ratios.

In this analysis, we studied (e,$e'p$) and (e,$e'n$) quasi-elastic knock-out event samples measured in two kinematical regions, corresponding to electron scattering from high-initial-momentum ($p_i > k_F$) nucleons, presumably from an SRC pair, or from low-initial-momentum ($p_i < k_F$) nucleons, presumably from shell-model states.

Using these events, we derived both the ratio of A(e,$e'n$)/A(e,$e'p$) events for each region and the double ratio of high-momentum (SRC) to low-momentum (shell model) nucleons in nuclei relative to carbon $[A(e,e'x)_{high}/A(e,e'x)_{low}]/[^{12}C(e,e'x)_{high}/^{12}C(e,e'x)_{low}]$, where A stands for Al, Fe or Pb. The double ratio is simply an estimator for the

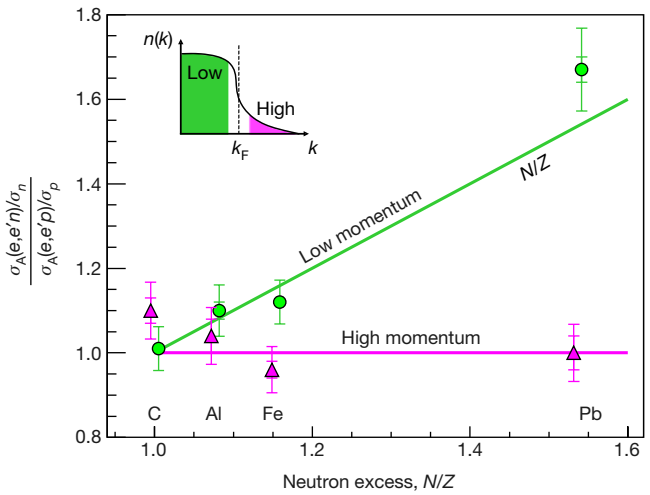

Fig. 2 | Relative abundances of high- and low-initial-momentum neutrons and protons. Reduced cross-section ratio, $[\sigma_A(e,e'n)/\sigma_n]/[\sigma_A(e,e'p)/\sigma_p]$, for low-momentum (green circles) and high-momentum (purple triangles) events. The inset illustrates a typical nuclear momentum distribution as a function of nucleon momentum, where 'low' and 'high' refer to the initial nucleon momentum. The lines show the simple N/Z behaviour (green), as expected from the number of neutrons and protons in the nucleus for low-momentum nucleons, and the prediction of the *np*-dominance model (purple; $[\sigma_A(e,e'n)/\sigma_n]/[\sigma_A(e,e'p)/\sigma_p] = 1$) for high-momentum nucleons. The inner error bars correspond to statistical uncertainties and the outer ones include both statistical and systematic uncertainties, both at the 1σ or 68% confidence level (see Supplementary Information).

increased fraction of SRC nucleons in an asymmetric nucleus compared to carbon. We used carbon as a reference because it is a well studied, medium-mass symmetric nucleus and has similar average density to the other nuclei measured here. In addition, forming cross-section ratios relative to carbon significantly reduces the effects of detector acceptance and efficiency corrections (see Supplementary Information). For each kinematical setting, we used the same selection criteria on the detected scattered electron and associated knocked-out nucleon to select quasi-elastic A$(e,e'p)$ and A$(e,e'n)$ events.

Low-initial-momentum events are characterized by low missing energy and low missing momentum ($E_{miss} < 80$–90 MeV and $p_{miss} = |\boldsymbol{p}_{miss}| < 250$ MeV c^{-1}, where c is the speed of light in vacuum; see Supplementary Information). Because the neutron momentum resolution was not good enough to select these events directly, we developed a set of alternative constraints to select the same events by using the detected electron momentum and the knocked-out nucleon angle, which were unaffected by the neutron momentum resolution (see Methods).

Similarly, we selected the high-initial-momentum events in two steps. We first selected quasi-elastic events with a leading nucleon by setting conditions on the energy and momentum transfer and requiring that the outgoing nucleon be emitted with most of the transferred momentum in the general direction of the momentum transfer. We then selected high-initial-momentum events by requiring large missing momentum ($p_{miss} > 300$ MeV c^{-1}). These selection criteria ensured that the electron interacted with a single high-initial-momentum proton or neutron in the nucleus[2,3,12]. Lastly, we optimized the nucleon-momentum-dependent conditions to account for the neutron momentum reconstruction resolution and corrected for any remaining bin-migration effects (see Methods).

To verify the neutron detection efficiency, detector acceptance corrections and event selection method, we extracted the neutron-to-proton reduced cross-section ratio for carbon, for both high and low initial nucleon momenta: $[\sigma_{^{12}C}(e,e'n)/\sigma_n]/[\sigma_{^{12}C}(e,e'p)/\sigma_p]$ (that is, the ratio of measured cross-sections for the scattering of electrons from carbon, scaled by the known elastic-scattering electron–neutron, σ_n, and electron–proton, σ_p, cross-sections). Figure 2 shows that these two measured cross-section ratios are consistent with unity, as expected for a symmetric nucleus. This shows that in both high- and low-initial-momentum kinematics, we have restricted the reaction mechanisms to primarily quasi-elastic scattering and have correctly accounted for the various detector-related effects.

For the other measured nuclei, the low-momentum $(e,e'n)/(e,e'p)$ reduced cross-section ratios grow approximately as N/Z, as expected from the number of neutrons (N) and protons (Z) in the nucleus. However, the high-momentum $(e,e'n)/(e,e'p)$ ratios are consistent with unity for all measured nuclei (see Fig. 2).

The struck nucleons could reinteract as they emerge from the nucleus, which we refer to as final-state interaction. Such an effect would cause the number of detected outgoing nucleons to decrease and also modify the angles and momenta of the knocked-out nucleons. These effects were estimated for symmetric and asymmetric nuclei using a relativistic Glauber framework, which showed that the decrease in the measured cross-section is similar for protons and neutrons and thus has a minor impact on cross-section ratios (see Methods).

Because rescattering changes the event kinematics, some of the events with high measured p_{miss} could have originated from electron scattering from a low-initial-momentum nucleon, which then rescattered, thus increasing p_{miss}. If the high-initial-momentum (high-p_{miss}) nucleons originated from electron scattering from the more numerous low-initial-momentum nucleons, followed by nucleon rescattering, then the high-momentum $(e,e'n)/(e,e'p)$ ratio would show the same N/Z dependence as the low-momentum ratio. Because the high-momentum $(e,e'n)/(e,e'p)$ ratio is independent of A, these nucleon-rescattering effects must be small in this measurement.

Thus, the constant $(e,e'n)/(e,e'p)$ high-momentum ratios indicate that there are equal numbers of high-initial-momentum protons and neutrons in asymmetric nuclei, even though these nuclei contain up to 50% more neutrons than protons. This observation is consistent with high-initial-momentum nucleons belonging primarily to *np* SRC pairs, even in neutron-rich nuclei[25]. This equality implies a greater fraction of high-initial-momentum protons. For example, if 20% of the 208 nucleons in ^{208}Pb have high initial momentum, then these consist of 21 protons and 21 neutrons. This corresponds to a high-momentum proton fraction of $21/82 \approx 25\%$ and a corresponding neutron fraction of only $21/126 \approx 17\%$.

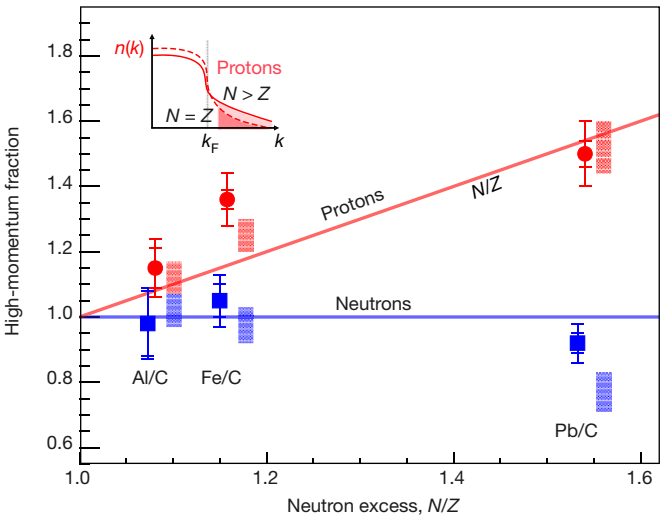

Fig. 3 | Relative high-momentum fractions for neutrons and protons. Red circles with error bars denote the double ratio of the number of $(e,e'p)$ high-momentum proton events to low-momentum proton events for nucleus A relative to carbon. The inner error bars are statistical and the outer ones include both statistical and systematic uncertainties, both at the 1σ or 68% confidence level. Blue squares with error bars show the same for neutron events. Red and blue rectangles show the range of predictions of the phenomenological *np*-dominance model for proton and neutron ratios, respectively (see Supplementary Information). The red line (high-momentum fraction equal to N/Z) and the blue line (high-momentum fraction equal to 1) are drawn to guide the eye. The inset demonstrates how adding neutrons to the target nucleus (solid red curve) increases the fraction of protons in the high-momentum tail (shaded region).

To quantify the relative fraction of high-momentum protons and neutrons in different nuclei with minimal experimental and theoretical uncertainties, we extracted the double ratio of $(e,e'x)$ high-initial-momentum to low-initial-momentum events for nucleus A relative to carbon for both protons and neutrons. We found that the fraction of high-initial-momentum protons increases by about 50% from carbon to lead (see Fig. 3).

Moreover, the corresponding fraction of high-initial-momentum neutrons seems to decrease by about 10% $\pm$ 5% (1σ). Nucleon rescattering, if substantial, should increase in larger nuclei and should affect protons and neutrons equally (see Methods). Because, unlike the proton ratio, the neutron ratio decreases slightly with mass number, this also rules out sizeable nucleon rescattering effects.

Figure 3 also shows the results of a simple phenomenological (that is, experiment-based) *np*-dominance model[5,26] that uses a mean-field momentum distribution at low momentum ($k < k_F$) and a scaled deuteron-like high-momentum tail. This model agrees with our data and also predicts momentum-sharing inversion, that is, on average protons move faster than neutrons in neutron-rich nuclei.

These results indicate that high-momentum nucleons and short-range two-body currents are universal and independent of the shell model. This conclusion holds for both the quasi-elastic and unitary-transformed pictures of the interaction and indicate that nuclei must be viewed in a scale-dependent way: nuclear structure at higher momentum scales and shorter distances must be described

using universal two-body physics, which is absent in an independent-particle shell-model picture using one-body operators.

The surprising fact that increasing the number of neutrons in a nucleus increases the fraction of high-initial-momentum protons (proposed in ref. [26] and bolstered by exact calculations of light nuclei[25] and calculations of heavier nuclei[27] and asymmetric nuclear matter[28]) has several broad implications. Neutron stars contain about 5%–10% protons and electrons in their central layers. Our results imply that the extreme neutron excess in a neutron star could dramatically increase the effects of short-distance currents on the protons, which could affect the cooling rate and equation of state of neutron stars[3,16].

There is evidence that the high-momentum nucleons associated with SRC pairs are responsible for the EMC effect, that is, the change in the quark distribution of nucleons bound in nuclei[1,13]. The EMC effect (named after the European Muon Collaboration) may result from two-body short-distance interactions that can be viewed as temporary high-density fluctuations of nucleon pairs in the nucleus, in which the internal structure of the affected nucleons is briefly modified[1]. If this mechanism indeed occurs, then the average proton in neutron-rich nuclei (the minority species) is more likely to belong to a correlated pair and should therefore be more modified than the average neutron (the majority species). Observing such increased modification of the proton structure in neutron-rich nuclei could shed new light on the currently unknown origin of these modifications of nuclear parton distribution functions.

Furthermore, the *np* dominance of SRC pairs and two-body short-distance currents in heavy nuclei has considerable implications in many areas of nuclear and particle physics (including nuclear correlation functions and the double-beta decay rate of nuclei[29], the nature of the repulsive core of the nucleon–nucleon interaction[2,6] and neutrino–nucleus interactions), where high-precision extraction of oscillation parameters and searches for new physics beyond the standard model require detailed understanding of the nuclear ground state and neutrino-interaction operators[15].

Online content

Any Methods, including any statements of data availability and Nature Research reporting summaries, along with any additional references and Source Data files, are available in the online version of the paper at https://doi.org/10.1038/s41586-018-0400-z.

Received: 18 December 2017; Accepted: 13 June 2018;
Published online 13 August 2018.

1. Hen, O., Miller, G. A., Piasetzky, E. & Weinstein, L. B. Nucleon–nucleon correlations, short-lived excitations, and the quarks within. *Rev. Mod. Phys.* **89**, 045002 (2017).
2. degli Atti, C.C. In-medium short-range dynamics of nucleons: recent theoretical and experimental advances. *Phys. Rep.* **590**, 1–85 (2015).
3. Frankfurt, L., Sargsian, M. & Strikman, M. Recent observation of short-range nucleon correlations in nuclei and their implications for the structure of nuclei and neutron stars. *Int. J. Mod. Phys. A* **23**, 2991–3055 (2008).
4. Subedi, R. et al. Probing cold dense nuclear matter. *Science* **320**, 1476–1478 (2008).
5. CLAS Collaboration. Momentum sharing in imbalanced Fermi systems. *Science* **346**, 614 – 617 (2014).
6. Korover, I. et al. Probing the repulsive core of the nucleon–nucleon interaction via the ^{4}He(*e*,*e*′*pN*) triple-coincidence reaction. *Phys. Rev. Lett.* **113**, 022501 (2014).
7. Piasetzky, E., Sargsian, M., Frankfurt, L., Strikman, M. & Watson, J. W. Evidence for strong dominance of proton–neutron correlations in nuclei. *Phys. Rev. Lett.* **97**, 162504 (2006).
8. Tang, A. et al. *n*–*p* short-range correlations from (*p*, 2*p* + *n*) measurements. *Phys. Rev. Lett.* **90**, 042301 (2003).
9. Fomin, N. et al., New measurements of high-momentum nucleons and short-range structures in nuclei. *Phys. Rev. Lett.* **108**, 092502 (2012).
10. CLAS Collaboration. Measurement of two- and three-nucleon short-range correlation probabilities in nuclei. *Phys. Rev. Lett.* **96**, 082501 (2006).
11. Frankfurt, L. L., Strikman, M. I., Day, D. B. & Sargsyan, M. Evidence for short-range correlations from high Q^2 (*e*,*e*′) reactions. *Phys. Rev. C* **48**, 2451 (1993).
12. Arrington, J., Higinbotham, D.W., Rosner, G. & Sargsian, M. Hard probes of short-range nucleon–nucleon correlations. *Prog. Part. Nucl. Phys.* **67**, 898–938 (2012).
13. Weinstein, L. B., Piasetzky, E., Higinbotham, D. W., Gomez, J., Hen, O. & Shneor, R. Short range correlations and the EMC effect. *Phys. Rev. Lett.* **106**, 052301 (2011).
14. Hen, O., Piasetzky, E. & Weinstein, L.B. New data strengthen the connection between short range correlations and the EMC effect. *Phys. Rev. C* **85**, 047301 (2012).
15. Gallagher, H., Garvey, G. & Zeller, G. P. Neutrino–nucleus interactions. *Annu. Rev. Nucl. Part. Sci.* **61**, 355–378 (2011).
16. Li, B. A., Cai, B. J., Chen, L.W. & Xu, J. Nucleon effective masses in neutron-rich matter. *Prog. Part. Nucl. Phys.* **99**, 29–119 (2018).
17. Caurier, E., Martínez-Pinedo, G., Nowacki, F., Poves, A. & Zuker, A. P. The shell model as a unified view of nuclear structure. *Rev. Mod. Phys.* **77**, 427–488 (2005).
18. Kelly, J. J. Nucleon knockout by intermediate-energy electrons. *Adv. Nucl. Phys.* **23**, 75–294 (1996).
19. Dickhoff, W. H. & Barbieri, C. Self-consistent Green's function method for nuclei and nuclear matter. *Prog. Part. Nucl. Phys.* **52**, 377–496 (2004).
20. Carlson, J. et al., Quantum Monte Carlo methods for nuclear physics. *Rev. Mod. Phys.* **87**, 1067–1118 (2015).
21. Frankfurt, L. L. & Strikman, M. I. High-energy phenomena, short-range nuclear structure and QCD. *Phys. Rep.* **76**, 215–347 (1981).
22. Bogner, S. K. & Roscher, D. High-momentum tails from low-momentum effective theories. *Phys. Rev. C* **86**, 064304 (2012).
23. More, S. N., Bogner, S. K. & Furnstahl, R. J. Scale dependence of deuteron electrodisintegration. *Phys. Rev. C* **96**, 054004 (2017).
24. Mecking, B. A. et al. The CEBAF large acceptance spectrometer (CLAS). *Nucl. Instrum. Methods A* **503**, 513–553 (2003).
25. Wiringa, R. B., Schiavilla, R., Pieper, S. C. & Carlson, J. Nucleon and nucleon-pair momentum distributions in A≤12 nuclei. *Phys. Rev. C* **89**, 024305 (2014).
26. Sargsian, M.M. New properties of the high-momentum distribution of nucleons in asymmetric nuclei. *Phys. Rev. C* **89**, 034305 (2014).
27. Ryckebusch, J., Vanhalst, M. & Cosyn, W. Stylized features of single-nucleon momentum distributions. *J. Phys. G* **42**, 055104 (2015).
28. Rios, A., Polls, A. & Dickhoff, W. H. Depletion of the nuclear Fermi sea. *Phys. Rev. C* **79**, 064308 (2009).
29. Kortelainen, M. and Suhonen, J. Nuclear matrix elements of $0\nu\beta\beta$ decay with improved short-range correlations. *Phys. Rev. C* **76**, 024315 (2007).

Acknowledgements This work was supported by the US Department of Energy (DOE), contract number DEAC05-06OR23177, under which Jefferson Science Associates, LLC, operates the Thomas Jefferson National Accelerator Facility; by the National Science Foundation, the Israel Science Foundation; the Chilean Comisión Nacional de Investigación Científica y Tecnológica; the French Centre National de la Recherche Scientifique and Commissariat a l'Energie Atomique; the French–American Cultural Exchange; the Italian Istituto Nazionale di Fisica Nucleare; the National Research Foundation of Korea; and the UK Science and Technology Facilities Council.

Reviewer information *Nature* thanks T. Aumann, D. Phillips and the other anonymous reviewer(s) for their contribution to the peer review of this work.

Author contributions The CEBAF large acceptance spectrometer was designed and constructed by the CLAS Collaboration and Jefferson Laboratory. Data processing and calibration, Monte Carlo simulations of the detector and data analyses were performed by a large number of CLAS Collaboration members, who also discussed and approved the scientific results. The analysis presented here was performed by M. Duer with input from O. Hen, E. Piasetzky and L. B. Weinstein and reviewed by the CLAS Collaboration.

Competing interests The authors declare no competing interests.

Additional information
Supplementary information is available for this paper at https://doi.org/10.1038/s41586-018-0400-z.
Reprints and permissions information is available at http://www.nature.com/reprints.
Publisher's note: Springer Nature remains neutral with regard to jurisdictional claims in published maps and institutional affiliations.

The CLAS Collaboration
M. Duer[1], O. Hen[2*], E. Piasetzky[1], H. Hakobyan[3], L. B. Weinstein[4], M. Braverman[1], E. O. Cohen[1], D. Higinbotham[5], K. P. Adhikari[6], S. Adhikari[7], M. J. Amaryan[4], J. Arrington[8], A. Ashkenazi[2], J. Ball[9], I. Balossino[10], L. Barion[10], M. Battaglieri[11], V. Batourine[5,12], A. Beck[2], I. Bedlinskiy[13], A. S. Biselli[14,15], S. Boiarinov[5], W. J. Briscoe[16], W. K. Brooks[3,5], S. Bueltmann[4], D. Bulumulla[4], V. D. Burkert[5], F. Cao[17], D. S. Carman[5], A. Celentano[11], G. Charles[4], T. Chetry[18], G. Ciullo[10,19], L. Clark[20], B. A. Clary[17], P. L. Cole[5,21,22], M. Contalbrigo[10], O. Cortes[21], V. Crede[23], R. Cruz-Torres[2], A. D'Angelo[24,25], N. Dashyan[26], R. De Vita[11], E. De Sanctis[27], M. Defurne[9], A. Deur[5], C. Djalali[28], G. Dodge[4], R. Dupre[29], H. Egiyan[5], A. El Alaoui[3], L. El Fassi[6], P. Eugenio[23], R. Fersch[30,31], A. Filippi[32], T. A. Forest[21], G. Gavalian[5,33], Y. Ghandilyan[26], S. Gilad[2], G. P. Gilfoyle[34], K. L. Giovanetti[35], F. X. Girod[5], E. Golovatch[36], R. W. Gothe[28], K. A. Griffoen[31], L. Guo[5,7], N. Harrison[5], M. Hattawy[8], F. Hauenstein[4], K. Hafidi[8], K. Hicks[18], M. Holtrop[33], C. E. Hyde[4], Y. Ilieva[16,28], D. G. Ireland[20],

B. S. Ishkhanov[36], E. L. Isupov[36], K. Joo[17], M. L. Kabir[6], D. Keller[37], G. Khachatryan[26], M. Khachatryan[4], M. Khandaker[38], A. Kim[17], W. Kim[12], A. Klein[4], F. J. Klein[22], I. Korover[1], S. E. Kuhn[4], L. Lanza[24], G. Laskaris[2], P. Lenisa[10], K. Livingston[20], I. J. D. MacGregor[20], C. Marchand[9], N. Markov[17], B. McKinnon[20], S. Mey-Tal Beck[2], T. Mineeva[3], M. Mirazita[27], V. Mokeev[5,36], R. A. Montgomery[20], A. Movsisyan[10], C. Munoz-Camacho[29], B. Mustapha[8], S. Nadeeshani[4], P. Nadel-Turonski[5], S. Niccolai[29], G. Niculescu[35], M. Osipenko[11], A. I. Ostrovidov[23], M. Paolone[39], E. Pasyuk[5], M. Patsyuk[2], A. Papadopoulou[2], K. Park[5,12], D. Payette[4], W. Phelps[7], O. Pogorelko[13], J. Poudel[4], J. W. Price[40], S. Procureur[9], Y. Prok[4,37], D. Protopopescu[20], M. Ripani[11], A. Rizzo[24,25], G. Rosner[20], P. Rossi[5,27], F. Sabatié[9], A. Schmidt[2], C. Salgado[38], B. A. Schmookler[2], R. A. Schumacher[15], E. P. Segarra[2], Y. G. Sharabian[5], G. D. Smith[41], D. Sokhan[20], N. Sparveris[39], S. Stepanyan[5], S. Strauch[16,28], M. Taiuti[42], J. A. Tan[12], M. Ungaro[5,43], H. Voskanyan[26], E. Voutier[29], D. P. Watts[41], X. Wei[5], N. Zachariou[41], J. Zhang[37], X. Zheng[8,37] & Z. W. Zhao[4]

[1]Tel Aviv University, Tel Aviv, Israel. [2]Massachusetts Institute of Technology, Cambridge, MA, USA. [3]Universidad Técnica Federico Santa María, Valparaíso, Chile. [4]Old Dominion University, Norfolk, VA, USA. [5]Thomas Jefferson National Accelerator Facility, Newport News, VA, USA. [6]Mississippi State University, Missisippi State, MS, USA. [7]Florida International University, Miami, FL, USA. [8]Argonne National Laboratory, Argonne, IL, USA. [9]IRFU, CEA, Université Paris-Saclay, Gif-sur-Yvette, France. [10]INFN, Sezione di Ferrara, Ferrara, Italy. [11]INFN, Sezione di Genova, Genova, Italy. [12]Kyungpook National University, Daegu, South Korea. [13]Institute of Theoretical and Experimental Physics, Moscow, Russia. [14]Fairfield University, Fairfield, CT, USA. [15]Carnegie Mellon University, Pittsburgh, PA, USA. [16]The George Washington University, Washington, DC, USA. [17]University of Connecticut, Storrs, CT, USA. [18]Ohio University, Athens, OH, USA. [19]Università di Ferrara, Ferrara, Italy. [20]University of Glasgow, Glasgow, UK. [21]Idaho State University, Pocatello, ID, USA. [22]Catholic University of America, Washington, DC, USA. [23]Florida State University, Tallahassee, FL, USA. [24]INFN, Sezione di Roma Tor Vergata, Rome, Italy. [25]Università di Roma Tor Vergata, Rome, Italy. [26]Yerevan Physics Institute, Yerevan, Armenia. [27]INFN, Laboratori Nazionali di Frascati, Frascati, Italy. [28]University of South Carolina, Columbia, SC, USA. [29]Institut de Physique Nucléaire, CNRS/IN2P3 and Université Paris Sud, Orsay, France. [30]Christopher Newport University, Newport News, VA, USA. [31]College of William and Mary, Williamsburg, VA, USA. [32]INFN, Sezione di Torino, Torino, Italy. [33]University of New Hampshire, Durham, NH, USA. [34]University of Richmond, Richmond, VA, USA. [35]James Madison University, Harrisonburg, VA, USA. [36]Skobeltsyn Institute of Nuclear Physics, Lomonosov Moscow State University, Moscow, Russia. [37]University of Virginia, Charlottesville, VA, USA. [38]Norfolk State University, Norfolk, VA, USA. [39]Temple University, Philadelphia, PA, USA. [40]California State University, Carson, CA, USA. [41]Edinburgh University, Edinburgh, UK. [42]Università di Genova, Genova, Italy. [43]Rensselaer Polytechnic Institute, Troy, NY, USA. *e-mail: hen@mit.edu

METHODS

Analysis details. The A(e,$e'p$) and A(e,$e'n$) event samples were selected by determining the common angular region for detecting both protons and neutrons, correcting for their detection efficiencies and accounting for the different momentum resolutions. Neutron momenta were determined to an uncertainty of about 10%–15% from their time of flight, which was measured using the CLAS electromagnetic calorimeter. Proton momenta were determined to an uncertainty of about 1% from the curvature of their trajectories in the CLAS magnetic field.

We accounted for the momentum resolution difference by: (1) selecting the desired A(e,$e'p$) events in high- and low-momentum kinematics, (2) 'smearing' the proton momentum for each event using the measured neutron momentum resolution, and (3) using unsmeared and smeared A(e,$e'p$) event samples to study bin migration effects and optimize the event selection criteria. This process results in a smeared event sample with as many of the 'original' A(e,$e'p$) events as possible (that is, high selection efficiency) and as few other events as possible (that is, high purity). We used the smeared proton momenta in the final selection of A(e,$e'p$) events for consistency with the A(e,$e'n$) analysis.

The final event sample contains about 85%–90% of the desired sample with about 15% contamination, resulting in less than about 5% more events in our sample. This 5% cross-section correction caused a correction of less than 1% to the ratios between different nuclei. We assigned systematic uncertainties equal to these corrections. See Supplementary Information for additional details.

Non-quasi-elastic reaction mechanisms and data interpretation. Because the measurement detects only the final-state particles, we need to include different reaction mechanisms to infer information about the initial nuclear state. In addition to quasi-elastic electron scattering from a single nucleon, the full reaction mechanism could include contributions from meson-exchange currents, isobar currents (exciting the struck nucleon to an excited state) and elastic and inelastic nucleon rescattering (final-state interactions, FSIs). In the case of high missing momentum, elastic FSIs include rescattering between the nucleons of the pair or with the residual system. The relative contribution of these reaction mechanisms, as compared to the quasi-elastic reaction of interest, strongly depends on the reaction kinematics[2,3,12,30,31]. Minimizing non-quasi-elastic reaction mechanisms also reduces their interference with the quasi-elastic reaction.

The high-missing-momentum measurement reported here was carried out using largely anti-parallel kinematics with high Q^2 and $x_B > 1$ (Q^2, four-momentum transfer squared; x_B, Bjorken variable). This kinematical region minimizes non-quasi-elastic reaction mechanisms as follows[2,3,12,31]: (i) meson-exchange currents are suppressed by a factor of $1/Q^2$ compared to SRC pair breakup, and their contribution in our kinematics is small; and (ii) isobar currents are suppressed at $x_B > 1$, where the virtual photon transfers less energy and is less able to excite the nucleon to an isobar current for a given Q^2. Further, at large knock-out nucleon momenta, FSI effects can be calculated using a generalized eikonal approximation in a Glauber framework[12,31–34]. These calculations show that in our measurement, elastic FSIs are largely suppressed for mean-field knock-out. For SRC breakup, they are confined to nucleons in close proximity, and thus the largest part of the scattering cross-section can be attributed to SRC pairs[12,30].

This simple quasi-elastic picture, with suppressed FSIs, is strongly supported by the fact that it describes well both high-Q^2 electron-scattering data and high-energy proton data[7,8], which have very different reaction mechanisms. In addition, the results of the electron and proton-scattering experiments give consistent SRC-pair isospin ratios[4,7,8] and centre-of-mass momentum distributions[8,35].

Asymmetry dependence of reaction mechanisms. As protons and neutrons propagate through asymmetric nuclei, they encounter more neutrons than protons, which could lead to different FSI effects that do not cancel in the cross-section ratios. However, at the large Q^2 of this measurement, the pp and nn scattering cross-sections are almost identical, leading to a 1% difference between proton and neutron FSIs, as estimated quantitatively using a full relativistic multiple-scattering Glauber approximation calculation[31].

Data interpretation using unitary transformations. From a theoretical standpoint, one can describe the scattering reaction in one of two mathematically equivalent ways: (a) using one-body operators acting on a ground-state wavefunction with a high-momentum tail, as discussed in the main text, or (b) using unitary-transformed many-body operators acting on a 'mean-field' ground state without a considerable high-momentum tail[23]. In the latter case, the description of the ground state is simpler, but complicated many-body operators are needed to describe the electron–nucleus interaction that leads to the measured final state. Although this approach has been proven to be very efficient in describing long-distance and low-energy properties of nuclei, it is not clear yet if it is a cost-effective way to describe the measured short-distance physics in heavy nuclei. Therefore, we discuss our results predominantly in the framework of untransformed wavefunctions and interactions.

Data availability. The raw data from this experiment are archived in Jefferson Laboratory's mass-storage silo (https://scicomp.jlab.org/docs/node/9).

30. Frankfurt, L. L., Sargsian, M. M. & Strikman, M. I. Feynman graphs and generalized eikonal approach to high energy knock-out processes. *Phys. Rev. C* **56**, 1124 (1997).
31. Colle, C., Cosyn, W. & Ryckebusch, J. Final-state interactions in two-nucleon knockout reactions. *Phys. Rev. C* **93**, 034608 (2016).
32. Colle, C. et al. Extracting the mass dependence and quantum numbers of short-range correlated pairs from *A*(*e*,*e'p*) and *A*(*e*, *e'pp*) scattering. *Phys. Rev. C* **92**, 024604 (2015).
33. Dutta, D., Hafidi, K. & Strikman, M. Color transparency: past, present and future. *Prog. Part. Nucl. Phys.* **69**, 1–27 (2013).
34. CLAS Collaboration. Measurement of transparency ratios for protons from short-range correlated pairs. *Phys. Lett. B* **722**, 63–68 (2013).
35. Shneor, R. et al., Investigation of proton–proton short-range correlations via the ^{12}C(*e*,*e'pp*) reaction. *Phys. Rev. Lett.* **99**, 072501 (2007).